Three dimensional frequency analysis of bidirectional functionally graded thick cylindrical shells using a radial point interpolation method (RPIM)

Three dimensional frequency analysis of bidirectional functionally graded thick cylindrical shells using a radial point interpolation method (RPIM)

Reza Pilafkan [a 1], Peter D. Folkow [a,*], Mansour Darvizeh [b], Abolfazl Darvizeh [b]

[a] *Department of Applied Mechanics, Chalmers University of Technology, SE-412 96 Göteborg, Sweden*

[b] *Department of Mechanical Engineering, Guilan University, PO Box 3756, Rasht, Iran*

Key words: functionally graded (FG) cylindrical shell, radial point interpolation method (RPIM), eigenfrequency, eigenmode

1 Introduction

The investigation of the governing equations for cylindrical shells has been of great interest in the history of elastodynamic theory. Most work consider modeling of thin shells using simplified approximate theories (Leissa, 1973) due to the complexity of the exact three-dimensional theory. However, in order to obtain accurate results for thick shells there are needs to adopt the three-dimensional theory. In the case of homogeneous isotropic shells, such work are presented adopting the method due to Pochhammer (1876) and Chree (1889), e.g. (Gazis, 1958; Armenakas et al., 1969). More recent solutions to homogeneous cylindrical shells are presented using finite element methods (FEM) (Gladwell and Vijay, 1975; Wang and Williams, 1996; Loy and Lam, 1999; Buchanan and Yii, 2002), or series solution techniques (Hutchinson and

[1] Visiting researcher, present address see b)

* Corresponding author. Tel: +46 31 7721521, Fax: +46 31 772 3827.
Email addresses: rezapilafkan@yahoo.com (Reza Pilafkan), peter.folkow@chalmers.se (Peter D. Folkow), darvizeh@guilan.ac.ir (Mansour Darvizeh), adarvizeh@guilan.ac.ir (Abolfazl Darvizeh).

El-Azhari, 1986; McDaniel and Ginsberg, 1993; Hägglund and Folkow, 2008), while So and Leissa (1997) use Ritz analysis.

Works on inhomogeneous shells, notably functionally graded (FG) shells, have recently attracted much attention. Functionally graded materials (FGM) are composite materials made of two (or more) phases of material constituents, where the phase distribution varies continuously. The most used group of FGM consists of ceramic and metal phases. Such FGM were developed in the mid 1980s where the strength of the metal and the heat resistance of the ceramic made these materials well suited for high-temperature environments. FGM also possess a number of other advantages compared to other inhomogeneous materials such as improved residual stress distribution, higher fracture toughness, and reduced stress intensity factors. Hence, FGM are nowadays used in many different fields of engineering (Birman and Byrd, 2007; Shen, 2009). FG shells are studied using various hypotheses such as Love's theory (Loy et al., 1999; Pradhan et al., 2000), first order shear deformation theory (Kadoli and Ganesan, 2006; Ansari and Darvizeh, 2008; Tornabene et al., 2009), higher order theory (Patel et al., 2005) and three-dimensional theory (Vel, 2010; Asgari and Akhlaghi, 2011). Among the work using three-dimensional theory, a series solution technique is adopted by Vel (2010) while FEM is used by Asgari and Akhlaghi (2011).

The vast majority of papers on FG structures consider material gradation in one direction only. However, by developing structures that are multidirectional functionally graded, it is possible to design a material distribution that more efficiently fulfil engineering demands such as resisting high-temperature environment in several directions (Nemat-Alla, 2003). Another possible application is to optimize the material configuration for a specific purpose, e.g. to control eigenfrequencies. This latter case is the object for studying bidirectional functionally graded beams by Goupee and Vel (2006) and plates by Qian and Batra (2005). More recently, a bidirectional functionally shell is presented by Asgari and Akhlaghi (2011) for free-free boundary conditions.

The mentioned work on bidirectional functionally graded beams and plates (Goupee and Vel, 2006; Qian and Batra, 2005) use meshless methods (MM) such as the element free Galerkin (EFG) method and the meshless local Petrov-Galerkin (MLPG) method, respectively. Various other MM have also gained popularity for solving elastodynamic problems the last decade, e.g. the reproducing kernel particle method (RKPM) and point interpolation methods (PIM). Comprehensive descriptions of different MM are presented by Liu (2002); Liu and Gu (2005) and in a review paper by Nguyen et al. (2008).

In FEM the elements are connected together by nodes in a predefined manner, while MM use scattered nodes not forming a mesh. Moreover, the shape functions in MM are of higher order that can change for each point of inter-

est, contrary to predefined low order element shape functions often used in FEM. Hereby problems in FEM related to meshing and re-meshing (adaptive analysis) procedures are more easily treated by MM. The drawback in MM are that the computational cost is usually higher than FEM, and that several parameters may have to be chosen in a delicate way.

The PIM have a convenient property as their shape functions possess Kronecker delta behavior, which is not generally the case for all MM. Among the different approaches using PIM, the radial point interpolation method (RPIM) is a widely used method that is known to render stable codes for arbitrary nodal distributions. The RPIM has rather simple shape functions that are easy to differentiate. Results presented in the literature show that RPIM often has higher convergence rate and accuracy than traditional FEM (Liu and Gu, 2005). The radial basis functions in RPIM could be of different types, of which multiquadric (MQ) functions are the most used since being generally superior to other functions like the Gaussian radial function (EXP). It should be noted that these radial basis functions involve several parameters to be chosen manually. It is important to choose these carefully as they have pronounced effect on the accuracy (Wang and Liu, 2002a,b; Liu et al., 2003, 2005).

There are several reports on dynamic shells using MM. Homogeneous shells are studied using various shell theories adopting numerical methods such as the EFG method for Love's theory (Liu et al., 2002), a radial basis function method using Reddy's third order theory (Ferreira et al., 2006) and the natural neighbor radial point interpolation method (NNRPIM) adopting the three-dimensional equations of motion (Dinis et al., 2011). Concerning FG shells, first order shear deformation theories are presented in both Zhao et al. (2009) using an element-free *kp*-Ritz method, and by Roque et al. (2010) using a radial basis function method. Recently a review with emphasis on EFG and RKPM for plates and shells is presented by Liew et al. (2011).

There are to our knowledge no presented work using MM on dynamic three-dimensional equations for FG shells. The object of this paper is to use the RPIM with MQ radial basis functions on a bidirectional FG shell according to the three-dimensional dynamical equations of motion. Results for eigenfrequencies and eigenmodes are presented using different boundary conditions.

2 Governing equations

Consider a cylindrical shell of length L with inner radius r_i and outer radius r_o. Cylindrical coordinates are used with radial coordinate r, circumferential coordinate θ and axial coordinate z, where the corresponding displacement

fields are

$$\mathbf{u} = [u \;\; v \;\; w]^T. \tag{1}$$

The cylinder is inhomogeneous, isotropic and linearly elastic with density $\rho(r, \theta, z)$, elastic moduli $E(r, \theta, z)$ and Poisson's ratio $\nu(r, \theta, z)$. The elasto-dynamic shell equations are expressed

$$\mathbf{A}\boldsymbol{\sigma} = \rho\ddot{\mathbf{u}}, \tag{2}$$

where

$$\boldsymbol{\sigma} = [\sigma_{rr} \;\; \sigma_{\theta\theta} \;\; \sigma_{zz} \;\; \sigma_{r\theta} \;\; \sigma_{rz} \;\; \sigma_{\theta z}]^T, \tag{3}$$

and

$$\mathbf{A} = \begin{bmatrix} \partial/\partial r + 1/r & -1/r & 0 & 1/r\,\partial/\partial\theta & \partial/\partial z & 0 \\ 0 & 1/r\,\partial/\partial\theta & 0 & \partial/\partial r + 2/r & 0 & \partial/\partial z \\ 0 & 0 & \partial/\partial z & 0 & \partial/\partial r + 1/r & 1/r\,\partial/\partial\theta \end{bmatrix}. \tag{4}$$

The stress-strain relation is written

$$\boldsymbol{\sigma} = \mathbf{D}\boldsymbol{\epsilon}, \qquad \boldsymbol{\epsilon} = [\varepsilon_{rr} \;\; \varepsilon_{\theta\theta} \;\; \varepsilon_{zz} \;\; \gamma_{r\theta} \;\; \gamma_{rz} \;\; \gamma_{\theta z}]^T, \tag{5}$$

where

$$\mathbf{D} = \frac{E}{(1+\nu)(1-2\nu)} \begin{bmatrix} 1-\nu & \nu & \nu & 0 & 0 & 0 \\ \nu & 1-\nu & \nu & 0 & 0 & 0 \\ \nu & \nu & 1-\nu & 0 & 0 & 0 \\ 0 & 0 & 0 & (1-2\nu)/2 & 0 & 0 \\ 0 & 0 & 0 & 0 & (1-2\nu)/2 & 0 \\ 0 & 0 & 0 & 0 & 0 & (1-2\nu)/2 \end{bmatrix}. \tag{6}$$

The relation between strains and displacements are

$$\boldsymbol{\epsilon} = \mathbf{L}\mathbf{u}, \tag{7}$$

where the operator matrix $\mathbf{L}$ is defined

$$\mathbf{L} = \begin{bmatrix} \partial/\partial r & 0 & 0 \\ 1/r & 1/r\,\partial/\partial\theta & 0 \\ 0 & 0 & \partial/\partial z \\ 1/r\,\partial/\partial\theta & \partial/\partial r - 1/r & 0 \\ \partial/\partial z & 0 & \partial/\partial r \\ 0 & \partial/\partial z & 1/r\,\partial/\partial\theta \end{bmatrix}. \tag{8}$$

Now, assuming n nodes in the support domain for a specific point in the shell, the displacement field may be approximated through

$$\mathbf{u} = \mathbf{N}\hat{\mathbf{u}}, \qquad \hat{\mathbf{u}} = [u_1 \;\; v_1 \;\; w_1 \;\; \cdots \;\; u_n \;\; v_n \;\; w_n \;]^T. \tag{9}$$

Here the shape function matrix $\mathbf{N}$ used for the RPIM is discussed further in Section 3. Introducing the strain-displacement matrix operator $\mathbf{B} = \mathbf{LN}$ the strains and stresses can be written as

$$\boldsymbol{\epsilon} = \mathbf{B}\hat{\mathbf{u}}, \qquad \boldsymbol{\sigma} = \mathbf{DB}\hat{\mathbf{u}}. \tag{10}$$

Consequently, by adopting variational calculus, the resulting set of equations become

$$\mathbf{M}\ddot{\hat{\mathbf{u}}} + \mathbf{K}\hat{\mathbf{u}} = \mathbf{F}, \tag{11}$$

where

$$\begin{aligned} &\mathbf{M} = \int_V \rho\mathbf{N}^T\mathbf{N}\mathrm{d}V, \qquad \mathbf{K} = \int_V \mathbf{B}^T\mathbf{DB}\mathrm{d}V, \\ &\mathbf{F} = \int_V \mathbf{N}^T\mathbf{f}_V\,\mathrm{d}V + \int_A \mathbf{N}^T\mathbf{f}_A\,\mathrm{d}A. \end{aligned} \tag{12}$$

The force term $\mathbf{F}$ involves possible body forces $\mathbf{f}_V$ and surface forces $\mathbf{f}_A$.

3 Radial Point Interpolation Method (RPIM)

This section gives a brief description of the radial point interpolation method (RPIM) as presented in Liu and Gu (2005); Liu et al. (2005). Consider a scalar field $\eta(\mathbf{x})$ in a 3D domain Ω. Assume that N nodes at $\mathbf{x}_i$ $(i = 1, 2, \ldots, N)$ are distributed throughout Ω. The meshfree method is based on that the field $\eta(\mathbf{x})$ at any point $\mathbf{x}$ is interpolated using function values at field nodes within a local support domain of the point $\mathbf{x}$. As only the surrounding nodes effect

the field at that point, the nodes outside the domain have no influence on it. This is written as

$$\eta(\mathbf{x}) = \sum_{i=1}^{n} \Psi_i(\mathbf{x})\hat{\eta}_i = \mathbf{\Psi}^T(\mathbf{x})\hat{\boldsymbol{\eta}}, \tag{13}$$

where $n = n(\mathbf{x})$ is the number of nodes within the local support domain, while $\hat{\eta}_i$ is the nodal field variable and $\Psi_i(\mathbf{x})$ is the shape function at the ith node. Similar to FEM, the shape function possesses a Kronecker delta function property

$$\Psi_i(\mathbf{x}_j) = \delta_{ij} \Rightarrow \eta(\mathbf{x}_i) = \hat{\eta}_i, \tag{14}$$

and is of unity partition

$$\sum_{i=1}^{n} \Psi_i(\mathbf{x}) = 1. \tag{15}$$

Note that the support domains can have different shapes, although circular form is perhaps most often used. The shape functions are obtained using radial basis functions

$$\eta(\mathbf{x}) = \sum_{i=1}^{n} R_i(\mathbf{x})a_i + \sum_{j=1}^{m} P_j(\mathbf{x})b_j = \mathbf{R}^T(\mathbf{x})\mathbf{a} + \mathbf{P}^T(\mathbf{x})\mathbf{b}. \tag{16}$$

Here $R_i(\mathbf{x})$ are the n radial basis functions and $P_j(\mathbf{x})$ are the m polynomial basis functions in coordinates $\mathbf{x}$, while a_i and b_j are constants. The polynomial functions $P_j(\mathbf{x})$ are included to improve the accuracy and interpolation stability. The radial basis functions $R_i(\mathbf{x})$ depend on the distance s between $\mathbf{x}$ and a node at $\mathbf{x}_i$, that is

$$s = \sqrt{(x - x_i)^2 + (y - y_i)^2 + (z - z_i)^2}. \tag{17}$$

There are a number of radial basis functions given in the literature, and the multiquadric (MQ) function used here has the form

$$R_i(\mathbf{x}) = \left(s^2 + (\alpha_c d_c)^2\right)^q, \tag{18}$$

where the influence from the shape parameters α_c, d_c and q are investigated in the numerical examples. The polynomial basis functions are

$$\mathbf{P}(\mathbf{x}) = [1 \;\; x \;\; y \;\; z \;\; x^2 \;\; xy \;\; xz \;\; \cdots \;\; P_m(\mathbf{x}) \;\;]^T. \tag{19}$$

The coefficients a_i and b_j are derived next. Using Eq. (14) in Eq. (16) gives

$$\hat{\boldsymbol{\eta}} = \hat{\mathbf{R}}\mathbf{a} + \hat{\mathbf{P}}\mathbf{b}, \tag{20}$$

where the rows in these matrices consists of the vectors $\mathbf{R}^T(\mathbf{x}_i)$ and $\mathbf{P}^T(\mathbf{x}_i)$

$$\hat{\mathbf{R}} = \begin{bmatrix} R_1(\mathbf{x}_1) & R_2(\mathbf{x}_1) & \cdots & R_n(\mathbf{x}_1) \\ R_1(\mathbf{x}_2) & R_2(\mathbf{x}_2) & \cdots & R_n(\mathbf{x}_2) \\ \cdots & \cdots & \cdots & \cdots \\ R_1(\mathbf{x}_n) & R_2(\mathbf{x}_n) & \cdots & R_n(\mathbf{x}_n) \end{bmatrix}, \quad \hat{\mathbf{P}} = \begin{bmatrix} 1 & x_1 & y_1 & \cdots & P_m(\mathbf{x}_1) \\ 1 & x_2 & y_2 & \cdots & P_m(\mathbf{x}_2) \\ \cdots & \cdots & \cdots & \cdots & \cdots \\ 1 & x_n & y_n & \cdots & P_m(\mathbf{x}_n) \end{bmatrix}. \tag{21}$$

In addition to these n equations for the $(n+m)$ unknowns a_i and b_j, the needed m extra equations are obtained through

$$\hat{\mathbf{P}}^T \mathbf{a} = \mathbf{0}. \tag{22}$$

Hence, by solving Eq. (20) adopting Eq. (22) it is possible to express $\mathbf{a}$ and $\mathbf{b}$ in terms of $\hat{\boldsymbol{\eta}}$, which may be used in Eq. (16) to give a set of equation on the form Eq. (13).

3.1 RPIM for free vibrations of cylindrical shells

From now on, assume a fix frequency ansatz with frequency ω. Moreover, the material inhomogeneities are assumed to be independent of the circumferential coordinate θ. Consequently, the cylindrical shell displacement fields may be written

$$\begin{aligned} u(r,\theta,z,t) &= U(r,z)\cos(k\theta)\mathrm{e}^{\mathrm{i}\omega t}, \\ v(r,\theta,z,t) &= V(r,z)\sin(k\theta)\mathrm{e}^{\mathrm{i}\omega t}, \\ w(r,\theta,z,t) &= W(r,z)\cos(k\theta)\mathrm{e}^{\mathrm{i}\omega t}, \end{aligned} \tag{23}$$

where k is the circumferential wave number. Hereby, the different modes k become independent of each other, and can be treated separately. Note that $k = 0$ means the axisymmetric vibration. By mutually exchange the cose function to a sine function and vice verse, the pure torsional mode is obtained for $k = 0$. Adopting Eq. (23) for the node displacements $\hat{\mathbf{u}}$, the displacement shape function matrix $\mathbf{N}$ in Eq. (9) follows from Eq. (13) according to

$$\mathbf{N} = \begin{bmatrix} \Psi_1\cos(k\theta) & 0 & 0 & \cdots & \Psi_n\cos(k\theta) & 0 & 0 \\ 0 & \Psi_1\sin(k\theta) & 0 & \cdots & 0 & \Psi_n\sin(k\theta) & 0 \\ 0 & 0 & \Psi_1\cos(k\theta) & \cdots & 0 & 0 & \Psi_n\cos(k\theta) \end{bmatrix}, \tag{24}$$

where the shape functions $\Psi_i(r,z)$ are independent of θ. Hence, by using Eq. (24) in Eq. (11) for free vibrational problems without body forces, this results

in the standard eigenvalue problem

$$(\mathbf{K} - \omega^2 \mathbf{M})\hat{\mathbf{u}} = \mathbf{0}. \tag{25}$$

4 Numerical results

In order to illustrate the RPIM applied to vibrational problems on an inhomogeneous shell, eigenfrequencies for various boundary conditions are presented for a functionally graded material (FGM). The material consists of a metal and ceramic phase, which may be graded in two dimensions: r and z. Denote the metal volume fraction function $V_m(r, z)$ and the corresponding ceramic volume fraction $V_c(r, z) = 1 - V_m(r, z)$. These functions could be modeled in numerous ways, but as an illustration consider the simple case

$$V_m(r, z) = \left(\frac{r_o - r}{r_o - r_i}\right)^{n_r} \left(\frac{L - z}{L}\right)^{n_z}. \tag{26}$$

Here the power law exponents n_r and n_z are assumed to be non-negative real numbers. According to Eq. (26), a pure metal phase is obtained for $n_r = n_z = 0$, while a one-dimensional graded material is modeled by setting only one of the exponents to zero. The general bidirectional FG case corresponds to a continuously decreasing metal volume fraction as r and z increase, resulting in pure ceramic material at the outer radius $r = r_o$ and at the end $z = L$. Consequently this material constitution could be applicable on a shell where the outer surface and/or one of the ends are in a high temperature environment.

There are various methods to determine the material properties in FG materials. Among these the rule of mixture (Voigt model) is perhaps the simplest, while other theories such as the Mori-Tanaka model and the self-consistent model take microstructural aspects into account, see discussion in Shen (2009). The Voigt model assumes that the various effective material properties (denoted by Q) are proportional to the volume ratio according to

$$Q(r, z) = Q_m V_m(r, z) + Q_c V_c(r, z). \tag{27}$$

The Mori-Tanaka model assumes that the effective density $\rho(r, z)$ follow from (27), while the elastic variables are obtained through

$$\frac{K - K_c}{K_m - K_c} = \frac{V_m}{1 + (1 - V_m)\left(3(K_m - K_c)/(3K_c + \mu_c)\right)}, \tag{28}$$

$$\frac{\mu - \mu_c}{\mu_m - \mu_c} = \frac{V_m}{1 + (1 - V_m)(\mu_m - \mu_c)/(\mu_c + f)}, \tag{29}$$

where

$$f = \frac{\mu_c(9K_c + 8\mu_c)}{6(K_c + 2\mu_c)}. \tag{30}$$

Here K is the bulk modulus $K = \lambda + 2\mu/3$, where the Lamé parameters are $\lambda = E\nu/((1+\nu)(1-2\nu))$ and $\mu = E/(2(1+\nu))$. Although the results from the Voigt and the Mori-Tanaka models differ to some extent, the overall behavior illustrated in the figures below are similar for both theories. From now on, consider only the Mori-Tanaka model.

As for the materials studied, the metal phase is aluminum (Al) while the ceramic phase is silicon carbide (SiC), see properties in Table 1. This pronounced difference in elastic moduli E between materials imply that the eigenfrequencies are sensitive to the material constitution. Hereby the eigenfrequencies for shells made of pure SiC is almost 2.5 times the values for pure Al. Note that this case differ from the similar shell problem addressed by Asgari and Akhlaghi (2011), where there seem to be a confuse in the chosen material data.

Material	$E\,(GPa)$	$\rho\,(kg/m^3)$	ν
Al	70	2700	0.3
SiC	420	3100	0.15

Table 1
Material properties

In order to see the effects from different boundary conditions on the FG shell, the following four conditions are studied: clamped-clamped (CC), free-free (FF) and two types of simply supported-simply supported (SS1, SS2). The SS1 case is reported by Buchanan and Yii (2002)

$$v(r,\theta,z,t) = w(r,\theta,z,t) = 0, \quad \sigma_{rz}(r,\theta,z,t) = 0, \qquad z = 0, L, \tag{31}$$

while the SS2 is the standard shear diaphragm case (Armenakas et al., 1969)

$$u(r,\theta,z,t) = v(r,\theta,z,t) = 0, \quad \sigma_{zz}(r,\theta,z,t) = 0, \qquad z = 0, L. \tag{32}$$

The shell geometry is that of a thick shell with $r_o/r_i = 2$ and $L/r_o = 2$, also studied elsewhere (So and Leissa, 1997; Buchanan and Yii, 2002; Asgari and Akhlaghi, 2011).

In the RPIM scheme, the solution is obtained for each k according to the ansatz Eq. (23). The resulting twodimensional domain is discretized into regularly distributed node points in r and z directions; $n_r \times n_z$ nodes. The choice of RPIM parameters, as well as the number and distribution of nodes, are chosen

from comparing the eigenfrequencies when $n_r = n_z = 0$ to the results for homogeneous thick shells presented by So and Leissa (1997); Buchanan and Yii (2002) for CC, FF and SS1 boundary conditions. Here the RPIM parameters are obtained by systematically varying the parameter values for a specific node configuration (6×10 nodes), from which a set of constants are chosen that are believed to render the most accurate results. Concerning the numbers of polynomial basis functions m in Eq. (16), values in the interval $0 \leq m \leq 6$ are tested which seems to result in the best choice when $m = 3$. Hereby, the polynomial basis functions Eq. (19) becomes

$$\mathbf{P}(\mathbf{x}) = [1 \;\; r \;\; z \;\;]^T. \tag{33}$$

For the number of nodes n within the local support domain used in Eqs. (9), this is estimated by using a fix support domain radius $r_s = 2d_c$, where d_c is the average distance between nodal points. The remaining two parameters q and α_c in Eq. (18) are chosen as $q = 1.03$ and $\alpha_c = 2$ after trying several different combinations of similar values, compare Liu et al. (2003, 2005).

As for the number and distribution of nodes in the twodimensional domain, the number of terms for a certain accuracy depends on the circumferential wave number k and the mode number. Concentrating on the fundamental modes for each k as depicted in the Figures 1-8 below, convergence results for homogeneous CC and FF shells are presented in Tables 2 and 3 when $k = 0, 1, 2$. Here the nondimensional eigenfrequency $\Omega = \omega r_o \sqrt{\rho_m/\mu_m}$. Both tables show that these eigenfrequencies seem to converge to the exact values, which for CC is taken from Buchanan and Yii (2002) and for FF is from So and Leissa (1997). The tables show the converging tendencies using relative few nodes; using slightly more terms (notably in the r directions) also render the correct values for CC when $m = 2$ and for FF when $m = 1$ and $m = 2$. It is interesting to note that accurate results are obtained using rather few nodes, which indicates the efficiency of the meshless method. The results given in Tables 2–3 are obtained using up to about 150 nodes, whereas the results for the inhomogeneous shells presented in the plots below use up to about 300 nodes.

4.1 Frequency analysis for FG shells

The influence on the eigenfrequency using bidirectional FG shells are studied in this section. First study the lowest eigenfrequency for each circumferential wave number k associated with the four boundary conditions. Figures 1–4 show these eigenfrequencies for different FG constituents, that is different power law exponents as presented in Eq. (26). Figure 1 considers the pure metal case. All the four boundary conditions have a common eigenfrequency $\Omega = 1.57$ for the pure torsional mode at $k = 0$. The lowest eigenfrequency is for FF at

m	$n_r \times n_z$	Ω	m	$n_r \times n_z$	Ω	m	$n_r \times n_z$	Ω
0	3×12	1.574	1	3×12	1.325	2	3×12	1.602
	3×15	1.573		3×15	1.323		3×15	1.600
	3×18	1.571		3×18	1.321		3×18	1.598
	6×12	1.570		6×12	1.310		9×12	1.597
	6×15	1.571		6×15	1.308		9×15	1.589
	6×18	1.571		6×18	1.308		9×18	1.591
	Exact	1.571		Exact	1.308		Exact	1.594

Table 2
Convergence table for a homogeneous CC shell.

m	$n_r \times n_z$	Ω	m	$n_r \times n_z$	Ω	m	$n_r \times n_z$	Ω
0	3×12	1.574	1	3×12	1.537	2	3×12	0.919
	3×15	1.573		3×15	1.540		3×15	0.923
	3×18	1.571		6×12	1.577		6×12	0.945
	6×12	1.566		6×15	1.580		6×15	0.952
	6×15	1.570		9×12	1.596		9×12	0.964
	6×18	1.571		9×15	1.600		9×15	0.965
	Exact	1.571		Exact	1.604		Exact	0.970

Table 3
Convergence table for a homogeneous FF shell.

$k = 2$ where $\Omega = 0.97$. These results for CC, FF and SS1 are in line with the homogenous case presented by Buchanan and Yii (2002). Corresponding curves are presented for thin shells using approximate shell theories (Pradhan et al., 2000; Ansari and Darvizeh, 2008) . Note that the present work has the lowest eigenfrequency for FF among the boundary conditions for the presented cases $k \geq 2$, which is not the case for Pradhan et al. (2000). Next consider Figs. 2 and 3 for one-directional FGM in z and r directions, respectively. Clearly the eigenfrequencies increase as the ceramic phase influence increases. Generally, the influence due to a variation in n_r is more prominent than for varying n_z, as expected. However, this is not entirely the case for FF shells, as the lowest eigenfrequency when $k = 2$ is more or less the same in both Fig. 2 and Fig. 3, see more below. Finally Fig. 4 presents the results for a bidirectional FGM, where the eigenfrequencies in all cases are higher than in the previous plots. Note from Eq. (26) that the ceramic phase here clearly dominates over the metal phase. As an example, the $k = 0$ case gives $\Omega = 3.65$ while the pure ceramic case gives $\Omega = 3.82$ for all four boundary conditions. A common tendency in all the Figures 1–4 is that the two SS curves lie in between the lower FF curve and the higher CC curve, except for $k \leq 1$.

It is interesting to further examine the behavior for FF shells concerning the one-directional variation in r and z. To this end, consider Figure 5 which shows the lowest eigenfrequency when $k = 1$ for different n_r and n_z when $n_z = 0$ and $n_r = 0$, respectively. Here it is clear from the crossing of curves that there is a transition point at around $n_i = 8.5$ from where the power law exponent n_z influences the frequency level more prominently than n_r. Such transition points are also present for $k = 0$ and $k = 2$, not illustrated here. As a comparison to Fig. 5, the corresponding CC case is displayed in Fig. 6 showing no crossing of curves.

To see the influence of the variation of the power law exponents, it is possible to display various plots for the four boundary conditions. As there are similar tendencies for all boundary conditions, only the CC case is presented here. Figure 7 shows the lowest eigenfrequency for each circumferential wave number k when $n_z = 0$ and varying n_r. This plot clearly shows the increase in frequency as n_r increases. For each n_r the $k = 1$ mode has the lowest eigenfrequency; just as for homogeneous material (Buchanan and Yii, 2002). Other power law exponents could have be chosen, but the overall behavior is similar to the present case. Similar plots are presented using either approximate shell theories (Pradhan et al., 2000; Kadoli and Ganesan, 2006; Ansari and Darvizeh, 2008) or three-dimensional theory (Asgari and Akhlaghi, 2011). Note that the latter work studying FF thick shells using FEM does not display a local minimum at $k = 2$ (compare the present Figs. 1–4) which seems somewhat inconsistent considering the results in table form for homogeneous shells presented therein as well as by So and Leissa (1997); Buchanan and Yii (2002). As a final illustration, Figure 8 presents the lowest eigenfrequency for $k = 0$ in the case of bidirectional FGM. This plot clearly shows the increase in frequency as the power law exponents increase. A similar case for FF shells is given by Asgari and Akhlaghi (2011).

4.2 Mode shapes for FG shells

It is of interest to see how the mode shapes are influenced by the bidirectional FG variation. Consider only the modes for $k = 0$ as is reported in Buchanan and Yii (2002) for a homogeneous shell. Here the FF and SS1 boundary conditions are studied for four cases: $n_r = 0, n_z = 0$; $n_r = 2, n_z = 0$; $n_r = 0, n_z = 2$, and $n_r = 2, n_z = 2$. Figures 9–11 illustrate the eigenmodes related to the mode shapes $\Omega_{h,2}$–$\Omega_{h,4}$ for a homogeneous shell. Here, the modes related to the torsional mode $\Omega_{h,1}$ for a homogeneous shell are not illustrated due to the deformation nature. Note that the corresponding FG shell modes for SS1 are ordered in the same fashion as the homogeneous shell. However for a FF shell the modes for $n_r = 0, n_z = 2$ and $n_r = 2, n_z = 2$ are seen to be ordered differently. Here the third modes are of $\Omega_{h,2}$ type in these cases, and illus-

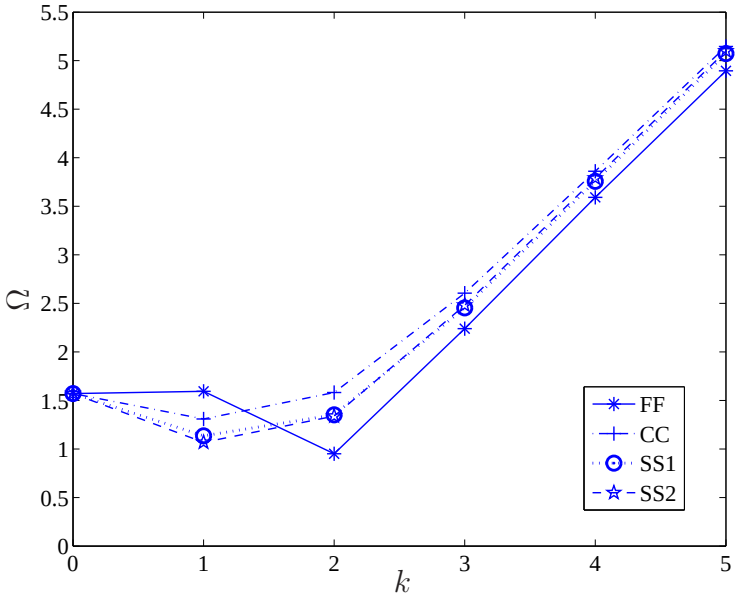

Fig. 1. First frequency Ω for each k associated with various boundary conditions; $n_r = 0, n_z = 0$.

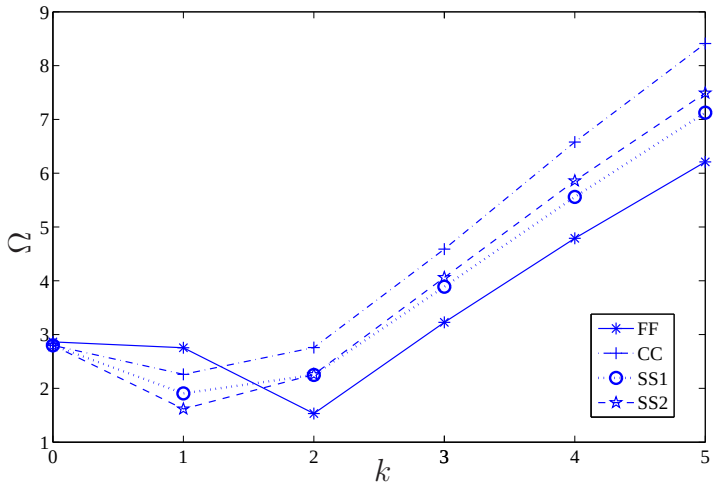

Fig. 2. First frequency Ω for each k associated with various boundary conditions; $n_r = 0, n_z = 2$.

trated in 9(a). For $n_r = 0, n_z = 2$ the torsional mode has the second lowest eigenfrequency, so the corresponding mode illustrated in 10(a) is for the lowest eigenfrequency. For $n_r = 2, n_z = 2$ the second mode is presented in 10(a). In each mode, the displacements are normalized so that the point originally at $(r = r_i, z = 0)$ has the same radial displacement for the four different FG cases.

It is clear from these plots that the FG variation has pronounced influence

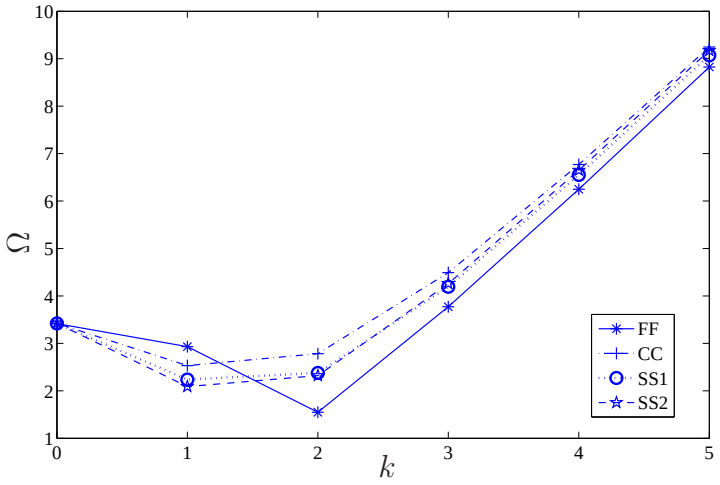

Fig. 3. First frequency Ω for each k associated with various boundary conditions; $n_r = 2, n_z = 0$.

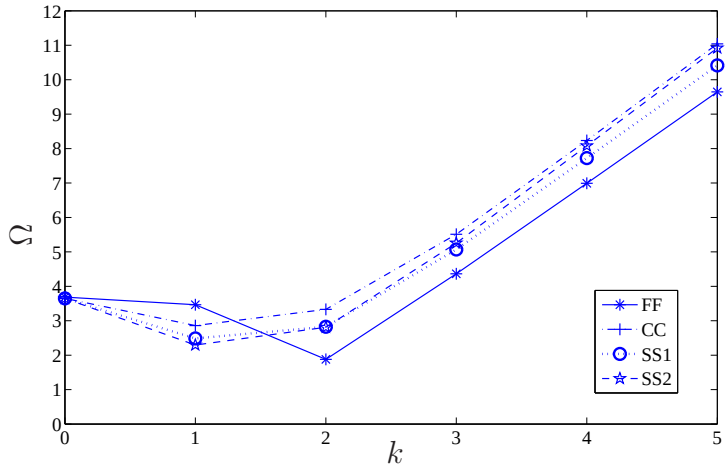

Fig. 4. First frequency Ω for each k associated with various boundary conditions; $n_r = 2, n_z = 2$.

on the mode shapes. Generally the modes using $n_r = 0, n_z = 0$ and $n_r = 2, n_z = 0$ are of the same type as expected, where the mode shapes posses the symmetric/antisymmetric behavior in line with Buchanan and Yii (2002). It is also clear that the curves where there is a variation in the z direction are similar; $n_r = 0, n_z = 2$, and $n_r = 2, n_z = 2$. In this latter case with variation in the z direction, the mode shapes are ordered differently for FF shells compared

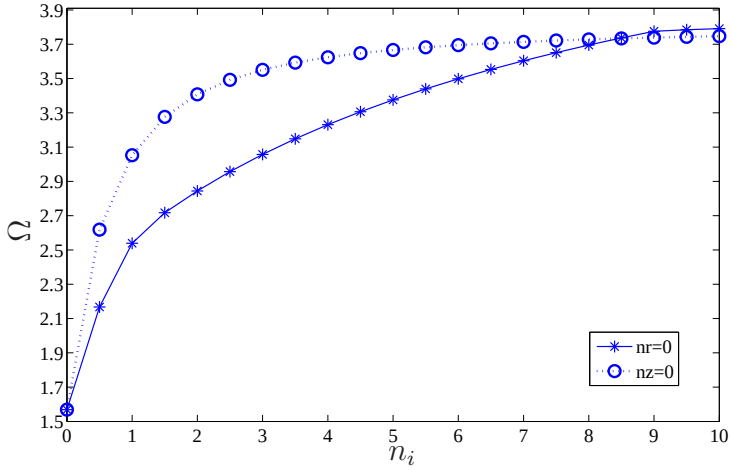

Fig. 5. First FF frequency Ω for $k = 1$ using various n_i where $i = r, z$.

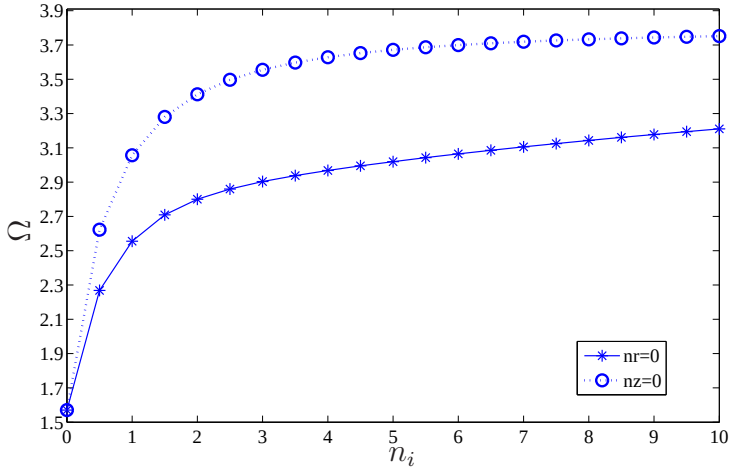

Fig. 6. First CC frequency Ω for $k = 1$ using various n_i where $i = r, z$.

to the $n_r = 0, n_z = 0$ and $n_r = 2, n_z = 0$ cases, as discussed above.

5 Conclusions

The paper illustrates the RPIM adopted on a thick shell using three-dimensional equations of motion. The shell is bidirectional FG where the variation is present in both the radial and the axial directions. Numerical results on eigenfrequencies are presented using four different boundary conditions, and results for eigenmodes are illustrated for two different boundary conditions. The effects from variation in radial and/or axial directions are illustrated in these figures.

This work shows that the RPIM is an efficient alternative to FEM when solving

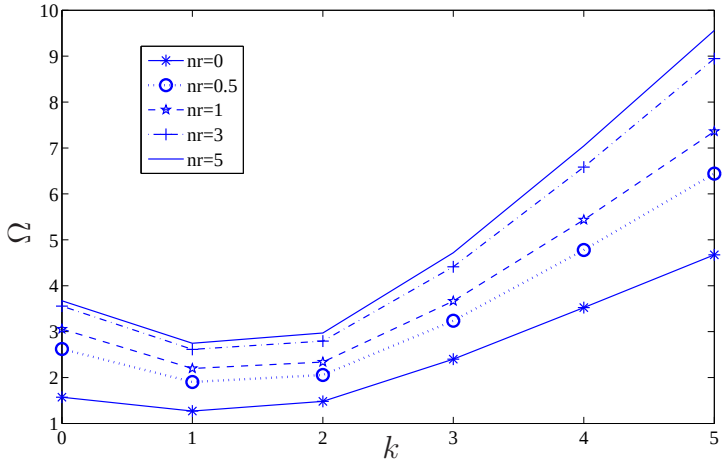

Fig. 7. First CC frequency Ω when $n_z = 0$ for each k using various n_r.

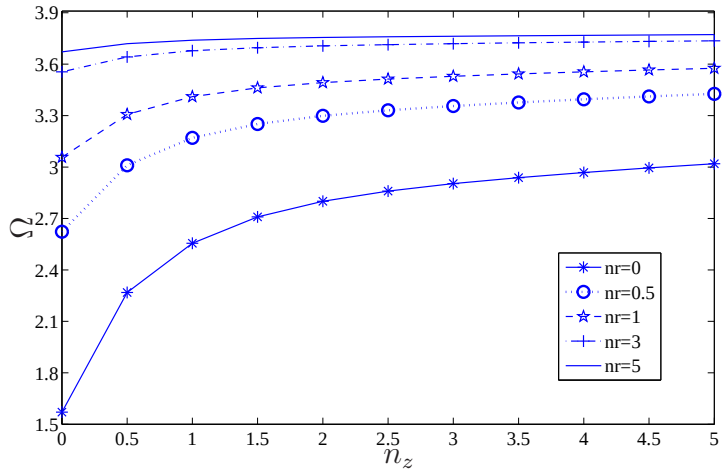

Fig. 8. First CC frequency Ω when $k = 0$ using various n_r and n_z.

dynamical shell problems. The virtue of this method is the absence of a mesh, the ease of handling both the boundary conditions and the coding procedure as a whole, resulting in a fast algorithm. The tuning of the parameters present in RPIM are obtained by comparing the results for a homogeneous shell to results given in the literature.

Possible applications of the present work concerns how to distribute the material constituents in two directions that more efficiently fulfil engineering purposes. Hereby it is possible to design structures that resist high-temperature environment in a structured manner. Future work includes optimization problems on choosing the material configuration for a specific purpose, e.g. to control eigenfrequencies.

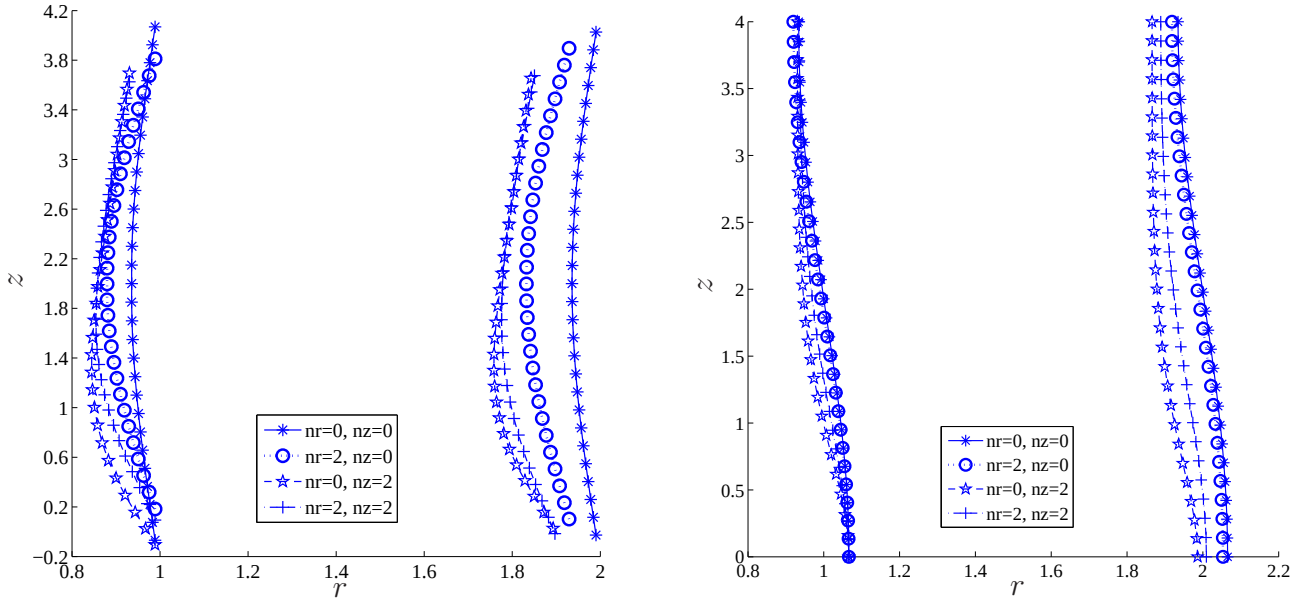

(a) FF (b) SS1

Fig. 9. Modeshapes for $k = 0$ related to $\Omega_{h,2}$; $r_i = 1$, $r_o = 2$ and $L = 4$.

References

R. Ansari and M. Darvizeh. Prediction of dynamic behaviour of FGM shells under arbitrary boundary conditions. *Comp. Str.*, 85:284–292, 2008.

A.E. Armenakas, D.C. Gazis, and G. Herrmann. *Free vibrations of circular cylindrical shells*. Pergamon Press, New York, 1969.

M. Asgari, M. Akhlaghi. Natural frequency analysis of 2D-FGM thick hollow cylinder based on three-dimensional elasticity equations. *Eur. J. Mech., A/Solids*, 30:72–81, 2011.

V. Birman and L.W. Byrd. Modeling and analysis of functionally graded materials and structures. *Appl. Mech. Rev.*, 60:195–216, 2007.

G.R. Buchanan and C.B.Y. Yii. Effect of symmetrical boundary conditions on the vibration of thick hollow cylinders. *Applied Acoustic*, 63:547–566, 2002.

D. Chree. The equations of an isotropic elastic cylinder in polar and cylindrical coordinates, their solutions and applications. *Transactions, Cambridge Philosophical Society*, 14:250, 1889.

L.M.J.S. Dinis, R.M. Natal Jorge, and J. Belinha. A natural neighbour meshless method with a 3D shell-like approach in the dynamic analysis of thin 3D structures. *Thin-Wall. Struct.*, 49:185–196, 2011.

A.J.M. Ferreira, C.M.C. Roque, and R.M.N. Jorge. Static and free vibration

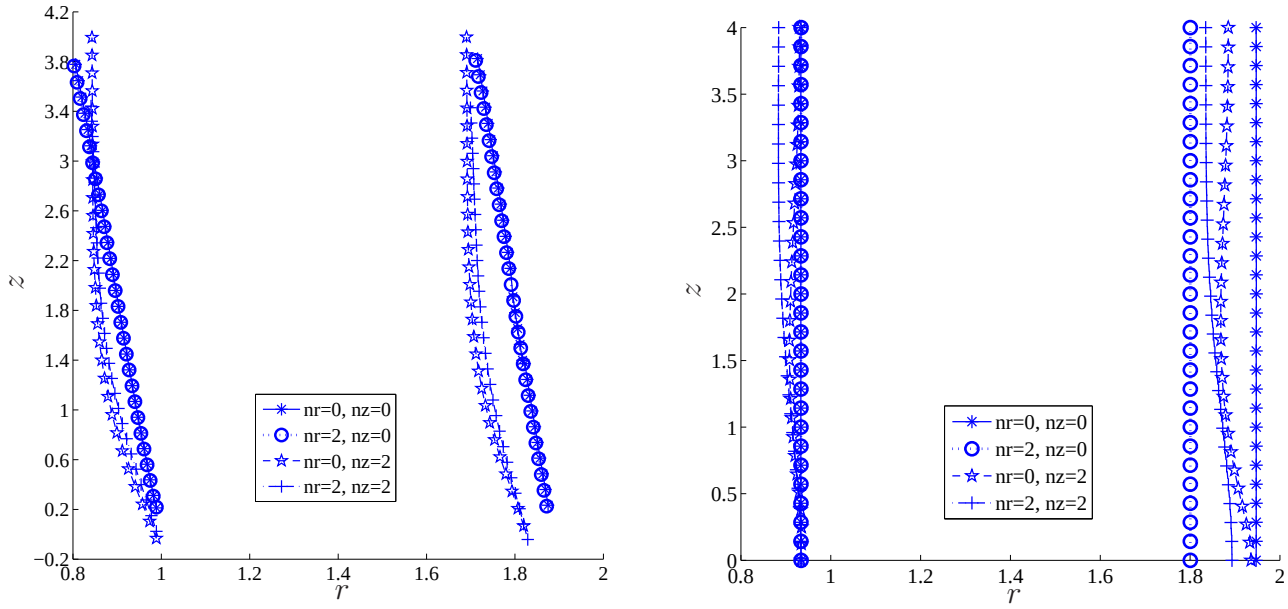

(a) FF (b) SS1

Fig. 10. Modeshapes for $k = 0$ related to $\Omega_{h,3}$; $r_i = 1$, $r_o = 2$ and $L = 4$.

analysis of composite shells by radial basis functions. *Eng. Anal. Bound. Elem.*, 30:719–733, 2006.

D.C. Gazis. Exact analysis of the plane-strain vibrations of thick-walled hollow cylinders. *J. Acoust. Soc. Am.*, 30:786–794, 1958.

G.M.L. Gladwell and D.K. Vijay. Natural frequencies of free finite-length circular cylinders. *J. Sound Vib.*, 42:387–397, 1975.

A.J. Goupee and S.S. Vel. Optimization of natural frequencies of bidirectional functionally graded beams. *Struct. Multidisc. Optim.*, 32:473–484, 2006.

A.M. Hägglund and P.D. Folkow. Dynamic cylindrical shell equations by power series expansions. *Int. J. Solids Struct.*, 45:4509–4522, 2008.

J.R. Hutchinson and S.A. El-Azhari. Vibrations of free hollow circular cylinders. *J. Appl. Mech.*, 53:641–646, 1986.

R. Kadoli and N. Ganesan. Buckling and free vibration analysis of functionally graded cylindrical shells subjected to a temperature specified boundary condition. *J. Sound Vib.*, 289:450–480, 2006.

A.W. Leissa. *Vibration of Shells*. NASA SP-288, Washington DC: US Government Printing Office, 1973.

K.M. Liew, X. Zhao, and A.J.M. Ferreira. A review of meshless methods for laminated and functionally graded plates and shells. *Comp. Str.*, 93:2031–

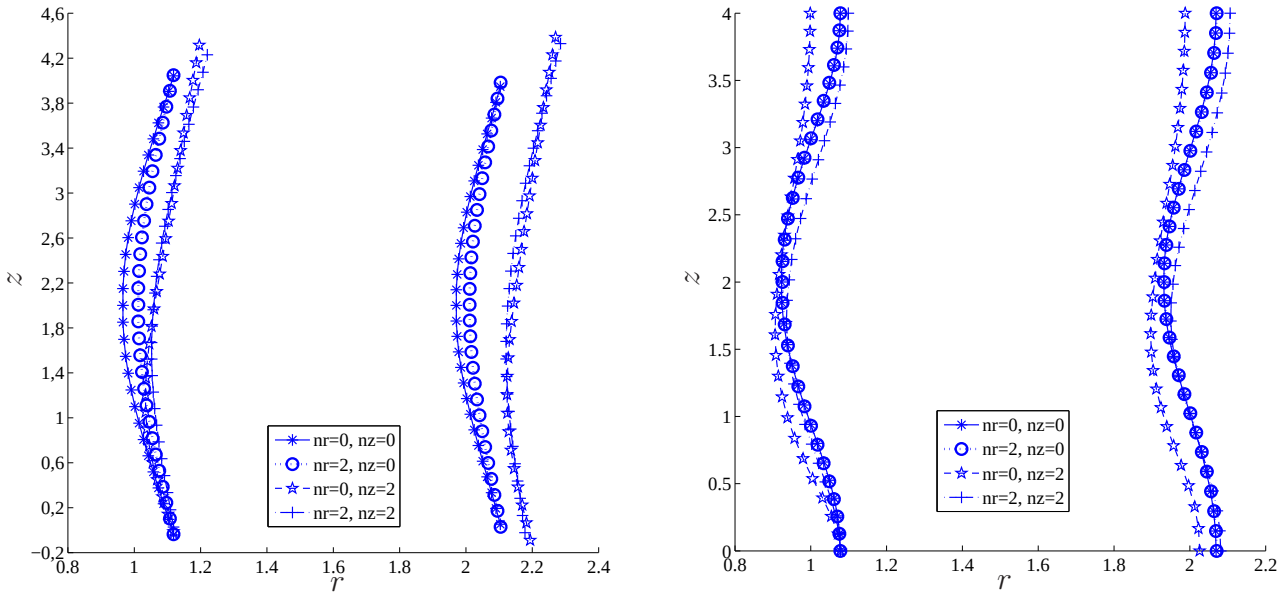

(a) FF (b) SS1

Fig. 11. Modeshapes for $k = 0$ related to $\Omega_{h,4}$; $r_i = 1$, $r_o = 2$ and $L = 4$.

2041, 2011.

G.R. Liu. *Meshfree Methods: Moving Beyond the Finite Element Method*. CRC Press, New York, 2002.

G.R. Liu, K.Y. Dai, K.M. Lim, and Y.T. Gu. A radial point interpolation method for simulation of two-dimensional piezoelectric structures. *Smart Mater. Struct.*, 12:171–180, 2003.

G.R. Liu and Y.T. Gu. *An Introduction to Meshfree Methods and Their Programming*. Springer, Dordrecht, 2005.

G.R. Liu, G.Y. Zhang, Y.T. Gu, and Y.Y. Wang. A meshfree radial point interpolation method (RPIM) for three-dimensional solids. *Comput. Mech.*, 36:421–430, 2005.

L. Liu, G.R. Liu, and V.B.C. Tan. Element free method for static and free vibration analysis of spatial thin shell structures. *Comput. Methods Appl. Mech. Engrg.*, 191:5923–5942, 2002.

C.T. Loy and K.Y. Lam. Vibration of thick cylindrical shells on the basis of three-dimensional theory of elasticity. *J. Sound Vib.*, 226:719–737, 1999.

C.T. Loy, K.Y. Lam, and J.N. Reddy. Vibration of functionally graded cylindrical shells. *Int. J. Mech. Sci.*, 41:309–324, 1999.

J.G. McDaniel and J.H. Ginsberg. Thickness expansions for higher-order effects in vibrating cylindrical shells. *J. Appl. Mech.*, 60:463–469, 1993.

M. Nemat-Alla. Reduction of thermal stresses by developing two-dimensional functionally graded materials. *Int. J. Solids Struct.*, 40:7339–7356, 2003.

V.P. Nguyen, T. Rabczuk, S. Bordas, and M. Duflot. Meshless methods: A review and computer implementation aspects. *Math. Comput. Simul.*, 79:763–813, 2008.

B.P. Patel, S.S. Gupta, M.S. Loknath, and C.P. Kadu. Free vibration analysis of functionally graded elliptical cylindrical shells using higher-order theory. *Comp. Str.*, 69:259–270, 2005.

L. Pochhammer. Über die fortpflanzungsgechwindigkeiten kleinerschwingungen in einem unbegrentzen isotropen kreiscylinder. *Z. Reine Angew. Math.*, 81:324–336, 1876.

S.C. Pradhan, C.T. Loy, K.Y. Lam, and J.N. Reddy. Vibration characteristic of functionally graded cylindrical shells under various boundary conditions. *Appl. Acoust.*, 61:111–129, 2000.

L.F. Qian and R.C. Batra. Design of bidirectional functionally graded plate for optimal natural frequencies. *J. Sound Vib.*, 280:415–424, 2005.

C.M.C. Roque, A.J.M. Ferreira, A.NA. Neves, G.E. Fasshauer, C.M.M. Soares, and R.M.N. Jorge. Dynamic analysis of functionally graded plates and shells by radial basis functions. *Mech. Adv. Mater. Struct.*, 17:636–652, 2010.

H.S. Shen. *Functionally graded materials: nonlinear analysis of plates and shells*. CRC Press, 2009.

J. So and A.W. Leissa. Free vibration of thick hollow circular cylinders from three-dimensional analysis. *J. Vibr. Acoust.*, 119:89–95, 1997.

F. Tornabene, E. Viola, and D.J. Inman. 2-D differential quadrature solution for vibration analysis of functionally graded conical, cylindrical shell and annular plate structures. *J. Sound Vib.*, 328:259–290, 2009.

S.S. Vel. Exact elasticity solution for the vibration of functionally graded anisotropic cylindrical shells. *Compos. Struct.*, 92:2712–2727, 2010.

H. Wang and K. Williams. Vibrational modes of thick cylinders of finite length. *J. Sound Vib.*, 191:955–971, 1996.

Y.Y. Wang and G.R. Liu. On the optimal shape parameters of radial basis functions used for 2-D meshless methods. *Comput. Appl. Mech. Eng.*, 191:2611–2630, 2002.

Y.Y. Wang and G.R. Liu. A point interpolation meshless method based on radial basis functions. *Int. J. Num. Meth. Eng.*, 54:1623–1648, 2002.

X. Zhao, Y.Y. Lee, and K.M. Liew. Thermoelastic and vibration analysis of functionally graded cylindrical shells. *Int. J. Mech. Sci.*, 51:694–707, 2009.